



# Numerical simulation of trickle bed reactors for biological methanation

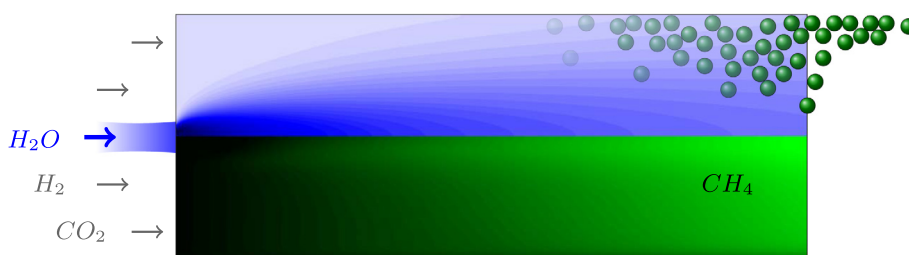
Simon Markthaler\*, Thomas Plankenbühler, Tobias Weidlich, Michael Neubert, Jürgen Karl

Friedrich-Alexander-Universität Erlangen-Nürnberg, Chair of Energy Process Engineering, Fürther Straße 244f, D-90429 Nürnberg, Germany

## HIGHLIGHTS

- Implementation of a CFD model based on the Eulerian-Eulerian method.
- Experimental data of the hydrodynamics, in particular liquid dispersion and holdup.
- Good agreement of simulation and experiments with regard to averaged macroscopic fluid flow.
- Spatial prediction of species adsorption and methane production.

## GRAPHICAL ABSTRACT



## ARTICLE INFO

### Article history:

Received 13 March 2020  
Received in revised form 22 April 2020  
Accepted 25 May 2020  
Available online 29 May 2020

### Keywords:

Biological methanation  
CFD  
Power-to-Gas  
Trickle-bed reactor  
Eulerian model  
Pseudo-continuous

## ABSTRACT

Biological methanation in trickle bed reactors is an auspicious approach to convert hydrogen and carbon dioxide into methane. In order to analyze this process, a comprehensive CFD model was implemented including multiphase flow, absorption, and reaction phenomena. The model is based on the Eulerian-Eulerian method. Experimental investigations and literature data serve as its validation. The experiments focused on the hydrodynamics of a trickle bed composed of clay granulate and the applied reactor enabled detailed measurements of radial liquid flow profiles and liquid holdup dependent on the overall volume flow rate. The simulation of liquid dispersion confirms the experimental results regarding averaged macroscopic fluid flow. However, liquid holdup is slightly underestimated by the computational model. In addition to the hydrodynamic investigation, simulation of biological methanation provide insight into mutual interactions between multiphase flow and biochemical conversion and present a methane production rate on the same order of magnitude as literature values.

© 2020 Elsevier Ltd. All rights reserved.

## 1. Introduction

Renewable energies are key technologies for sustainable energy supply with low greenhouse gas emissions. However, the integration of renewable power into global energy systems is challenging owing to the volatility of renewable energy sources. In particular, wind and solar power feature considerable fluctuations and require improved storage technologies to stabilize the electrical grid and maximize the harvest of renewable energies (Thema et al., 2016).

One way to tackle this volatility is chemical energy storage systems. The surplus electrical energy of wind and solar power can be

stored within chemical molecules, such as hydrogen ( $H_2$ ) or methane ( $CH_4$ ) – so-called “power-to-gas” (PtG) processes (Götz et al., 2016). In PtG, electrolysis dissociates water molecules by means of electrical current and produces hydrogen (Coutanceau et al., 2017). Subsequently, a methanation process can transform renewable hydrogen into methane. In comparison with hydrogen, methane exhibits two major benefits: higher volumetric energy density and the possibility of feeding large amounts of methane into the gas grid (Sterner and Stadler, 2014). The gas grid itself possesses high storage capacity and permits the utilization of methane for sector coupling, i.e. for power, heat and mobility applications.

Biological methanation is an emerging technology for the conversion of hydrogen and carbon dioxide ( $CO_2$ ) into methane. It involves a multiphase system with microorganisms, members of Archaea, present in the liquid phase (Thema et al., 2019). Due to

\* Corresponding author.

E-mail address: [simon.markthaler@fau.de](mailto:simon.markthaler@fau.de) (S. Markthaler).

## Nomenclature

### Roman

$a$	Distinct chamber in the reactor bottom [-]
$a_l$	Interfacial area [ $\text{m}^2/\text{m}^3$ ]
$a_s$	Specific surface area [ $\text{m}^2/\text{m}^3$ ]
$A_0$	Pre-exponential factor [ $\text{m}^3/(\text{mol}\cdot\text{s})$ ]
$A_R$	Cross-sectional area of the reactor [ $\text{m}^2$ ]
$c_l^i$	Concentration of species $l$ in phase $q$ [ $\text{mol}/\text{m}^3$ ]
$y^{\text{CH}_4}$	Methane concentration [vol.-%]
$d_p$	Particle diameter [m]
$D_R$	Reactor diameter [m]
$D_q^l$	Diffusivity of species $l$ in phase $q$ [ $\text{m}^2/\text{s}$ ]
$e$	Relative error of the grid solutions
$E_A$	Activation energy [J/mol]
$E_{\mu,q}; E_{p,q}$	Ergun parameter [-]
$E_{\mu}; E_p$	One-phase Ergun parameter [-]
$E\ddot{o}'$	Modified Eötvös number [-]; $E\ddot{o}' = \rho_L g d_p^2 \varepsilon^2 / (\sigma(1 - \varepsilon)^2)$
$f_e$	Wetting efficiency [-]
$f_\tau$	Friction factor [-]
$F_s$	Safety factor
$F_{bq}$	Interaction force from phase $b$ on phase $q$ [N/ $\text{m}^3$ ]
$F_{\text{int},q}$	Total phase interaction forces on phase $q$ [N/ $\text{m}^3$ ]
$F_{\text{disp},q}$	Dispersion forces on phase $q$ [N/ $\text{m}^3$ ]
$Fr_G$	Froude number [-]; $Fr_G = U_G / \sqrt{g d_p}$
$g$	Gravitational acceleration [ $\text{m}/\text{s}^2$ ]
$Ga'_G$	Modified Galileo number [-]; $Ga'_G = \rho_G^2 g d_p^3 / (\mu_G^2 (1 - \varepsilon)^3)$
$GCI$	Grid convergence index [-]
$GHSV$	Gas hourly space velocity [1/s]
$J_q$	Diffusive flux [ $\text{kg}/(\text{m}^2\text{s})$ ]
$k_f$	Reaction rate constant [ $\text{m}^3/(\text{mol}\cdot\text{s})$ ]
$k_q$	Mass transfer coefficient [m/s]
$K_{bq}$	Interaction coefficient [ $\text{kg}/(\text{m}^3\text{s})$ ]
$K_H^{l,px}$	Henry's law constant [Pa]
$\Delta L$	Trickle bed depth [m]
$M^l$	molecular weight [kg/mol]
$\dot{m}_L$	Liquid mass flow rate [kg/s]
$\dot{m}_{bq}^l$	Species mass transfer from phase from phase $b$ to phase $q$ [kg/s]
$(\dot{m}_L/A)_a$	Averaged liquid mass flux of chamber $a$ [ $\text{kg}/(\text{m}^2\text{s})$ ]
$MPR$	Methane production rate [ $\text{m}^3_{\text{N},\text{CH}_4}/(\text{m}^3\text{d})$ ] = [Normal cubic meter of methane/(cubic meter • day)]
$N$	Number of grid cells [-]
$p$	Pressure [Pa]
$p_{\text{Grid}}$	Order of convergence [-]
$r$	Radius [m]
$r$	Grid refinement [-]
$R_q^l$	Homogeneous reaction rate [ $\text{kg}/(\text{m}^3\text{s})$ ]
$Re'_L$	Modified Reynolds number [-]; $Re'_L = \rho_L d_p U_L / (\mu_L (1 - \varepsilon))$
$Re_p$	Particle Reynolds number [-]; Liquid: $Re_{p,L} = \rho_L d_p U_L / \mu_L$ ; Gas: $Re_{p,G} = \rho_G d_p U_G / \mu_G$

$S$	Spread factor [-]
$S_m$	Model spread factor [-]
$S_q$	Change in mass of phase $q$ due to heterogeneous reactions [ $\text{kg}/(\text{m}^3\text{s})$ ]
$S_q^l$	Heterogeneous reaction rate [ $\text{kg}/(\text{m}^3\text{s})$ ]
$T_0$	One-phase tortuosity [-]
$T_{q,}$	Tortuosity of phase $q$ [-]
$\vec{u}_G$	Modified gas velocity [m/s]
$u_{G,\text{in}}^{\text{crit}}$	Critical gas inlet velocity [m/s]
$\vec{u}_q$	Velocity of phase $q$ [m/s]
$U_q$	Superficial velocity of phase $q$ [m/s]
$u_{q,\text{in}}$	Inlet velocity of phase $q$ [m/s]
$\vec{u}_{bq}$	Mass transfer velocity [m/s]
$\vec{u}_{D,q}$	Drift velocity of phase $q$ [m/s]
$V$	Volume [ $\text{m}^3$ ]; $V = \sum_q V_q$
$V_R$	Global volume of the packing [ $\text{m}^3$ ]
$V_q$	Volume of phase $q$ [ $\text{m}^3$ ]
$\dot{V}_{\text{CH}_4,\text{in}}$	Methane volume flow rate at the inlet [ $\text{m}^3/\text{s}$ ]
$\dot{V}_{\text{CH}_4,\text{out}}$	Methane volume flow rate at the outlet [ $\text{m}^3/\text{s}$ ]
$\dot{V}_{G,\text{in}}$	Gas inlet volume flow rate [ $\text{m}^3/\text{s}$ ]
$\dot{V}_L$	Overall liquid volume flow rate [ $\text{m}^3/\text{s}$ ]
$x$	Coordinate axis alongside the trickle bed depth [m]
$x_q$	Characteristic length of phase $q$ [m]
$x_l$	Molar fraction of species $l$ [-]

### Greek

$\alpha$	Gas saturation [-]; $\alpha = V_G / (V_G + V_L)$
$\beta_L$	Liquid holdup [-]; $\beta_L = V_L / V_R$
$\beta_{L,\text{dyn}}$	Dynamic liquid holdup [-]; $\beta_{L,\text{dyn}} = V_{L,\text{dyn}} / V_R$
$\beta_{L,\text{Exp}}$	Liquid holdup, evaluated experimentally [-];
$\beta_{L,\text{stat}}$	Static liquid holdup [-]; $\beta_{L,\text{stat}} = V_{L,\text{stat}} / V_R$
$\varepsilon$	Porosity [-]; $\varepsilon = V_G / V_R$
$\varepsilon_{j(j+1)}$	Solution difference [m]
$\theta_q$	Volume fraction of phase $q$ [-]; $\theta_q = V_q / V$
$\mu_q$	Viscosity of phase $q$ [Pa s]
$\nu^l$	stoichiometric factor of species $l$ [-]
$\xi$	Wall distance [-]; $\xi = (R_R - r) / d_p$
$\rho_q$	Density of phase $q$ [ $\text{kg}/\text{m}^3$ ]
$\rho_{\text{H}_2\text{O}}$	Density of water [ $\text{kg}/\text{m}^3$ ]
$\dot{\rho}_{bq}$	Mass flow rate per volume element from phase $b$ to phase $q$ [ $\text{kg}/(\text{m}^3\text{s})$ ]; $\dot{\rho}_{bq} = \sum_l \dot{\rho}_{bq}^l$
$\dot{\rho}_{bq}^l$	Species transport per volume element from phase $b$ to phase $q$ [ $\text{kg}/(\text{m}^3\text{s})$ ]
$\sigma$	Surface tension [ $\text{kg}/\text{s}^2$ ]
$\tau$	Retention time [s]
$\psi$	Particle shape factor [-];
$\omega$	Relaxation factor
$\omega_q^l$	Mass fraction of species $l$ in phase $q$ [-]

concentration gradients between the different phases, the gaseous educts dissolve in the liquid phase. The microorganisms absorb the dissolved  $\text{H}_2$  and  $\text{CO}_2$  and convert them into  $\text{CH}_4$  (Fig. 1). Within the microorganism, enzymes catalyze the methanation reaction (Sabatier reaction) biochemically (Sterner and Stadler, 2014).



Trickle bed reactors provide high interfacial area and simplicity in operation. The liquid phase enters the reactor at the top and the gas phase is conducted in cocurrent or countercurrent flow

(Ranade et al., 2011). According to Burkhardt (2012), the microorganisms partially settle on the surface of the trickle bed particles and establish an immobilized biofilm.

To date, several studies have reported the effectiveness of biological methanation in trickle bed reactors (Rachbauer et al., 2016; Burkhardt and Busch, 2013; Burkhardt et al., 2015; Strübing et al., 2017; Dupnock and Deshusses, 2017; Weidlich et al., 2018). Rachbauer et al. (2016) intensively studied biogas upgrading and achieved  $\text{CO}_2$  conversion up to 96% and  $\text{CH}_4$  product gas concentrations of approximately 96 vol.-%. Burkhardt and Busch (2013) obtained even higher  $\text{CH}_4$  concentrations of 97.9 vol.-% and  $\text{H}_2$  conversion up to 99% applying a reactor design

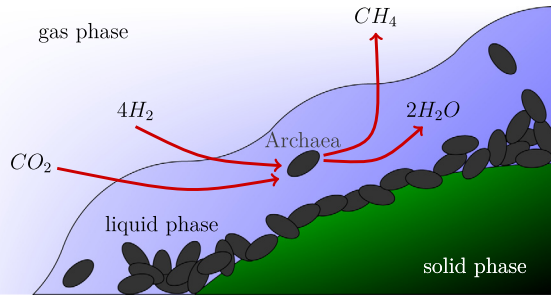


Fig. 1. Biological methanation by Archaea microorganisms.

with product gas recycle. However, wetting and nutrition of microorganisms differs locally with regions of insufficient nutrient supply and low microbial density (Dupnock and Deshusses, 2017). As a result, biological methanation currently suffers from low methane production rates (MPR) which necessitates large and expensive reactor systems (Bär et al., 2015). The optimization of biological methanation in trickle bed reactors is, therefore, of paramount importance in order to compete with chemically catalyzed methanation devices.

Simulation via computational fluid dynamics (CFD) is a promising avenue for reactor optimization. In recent history, efforts have been made to describe multiphase flows in trickle bed reactors by mathematical models and to predict phase interaction, pressure drop and liquid dispersion. The fundamentals of Ergun (1952) were transferred to a 1D approach by Attou et al. (1999) and refined by several authors (Iliuta and Larachi, 2005; Alopaeus et al., 2006; Lappalainen et al., 2009). Lappalainen et al. (2009) extended the model equations to 2D and 3D applications by introducing dispersion forces for different spatial directions. Following this work, Kim et al. (2016) and Janecki et al. (2016) have implemented similar modelling schemes which cover CFD trickle bed simulations of CO<sub>2</sub> amine absorption and oxidation of phenol, respectively.

To the best of our knowledge, there is no work that directly addresses numerical simulation of biological methanation in trickle bed reactors. Therefore, we developed a pseudo-continuous model, including the elaborations from the literature above, and extended the model equations with appropriate absorption and reaction kinetics for biological methanation.

On the basis of this CFD model, we performed simulations of two different scenarios. On the one hand, we computed a water–air system without absorption and reaction mechanisms. The results are directly compared to water–air experiments with a trickle bed of spherical clay granulate, which allow the validation of liquid dispersion and holdup. The experiments contain measurements of radial liquid flow profiles at different trickle bed depths of  $10\text{ cm} < \Delta L < 40\text{ cm}$  and different overall liquid mass flux values of  $\dot{m}_L/A_R = 1.2\text{ kg}/(\text{m}^2\text{s})$  to  $\dot{m}_L/A_R = 7.2\text{ kg}/(\text{m}^2\text{s})$ . On the other hand, we simulated biological methanation with feed gas composed of H<sub>2</sub> and CO<sub>2</sub> and analyzed the methane production rate with respect to literature data. Latter simulations do not only consider hydrodynamics of fluid flow, but also interfacial species transport and biochemical conversion.

### 1.1. Computational model

The computational model entails equations considering both multiphase flow and species transport. The flow conditions can be assumed to be laminar due to particle Reynolds numbers of  $Re_{p,G} < 64$  and  $Re_{p,L} < 170$  for the gas and liquid phase. These values are substantially below the transition to turbulence in between  $Re_p = 250 - 400$  (Ranade et al., 2011).

### 1.2. Multiphase flow

The model aligns with the mathematical formulation by Lappalainen et al. (2009) based on the Eulerian-Eulerian approach for Newtonian fluids. The Eulerian-Eulerian approach considers the phases as interpenetrating continua without resolving the exact location of the gas/liquid/solid interface (Alopaeus et al., 2006). Hence, the system is deemed pseudo-continuous. Such a model incorporates interactions by means of phase interaction forces  $\vec{F}_{int,q}$  and dispersion forces  $\vec{F}_{disp,q}$  in the governing equations. These equations account for mass and momentum conservation and need to be solved for the gas (G) and liquid (L) phase:

$$\frac{\partial \theta_q \rho_q}{\partial t} + \nabla \cdot (\theta_q \rho_q \vec{u}_q) = \dot{\rho}_{bq} + S_q \quad (2)$$

$$\begin{aligned} \frac{\partial}{\partial t} (\theta_q \rho_q \vec{u}_q) + \nabla \cdot (\theta_q \rho_q \vec{u}_q \vec{u}_q) \\ = -\theta_q \nabla p + \theta_q \mu_q \Delta \vec{u}_q + \theta_q \rho_q \vec{g} + \dot{\rho}_{bq} \vec{u}_{bq} + \vec{F}_{int,q} + \vec{F}_{disp,q} \end{aligned} \quad (3)$$

in which  $\theta_q$ ,  $\rho_q$ ,  $\mu_q$ , and  $\vec{u}_q$  refer to volume fraction, density, viscosity, and velocity of phase  $q$ , respectively. The solid phase remains immobile and can, thus, be neglected. In addition to the model by Lappalainen et al. (2009), which neglects interfacial mass transfer, the term  $\dot{\rho}_{bq}$  represents the mass flow rate per volume element from phase  $b$  into phase  $q$ . This interfacial mass transfer contributes to momentum balance with the velocity  $\vec{u}_{bq} = \vec{u}_q$  for  $\dot{\rho}_{bq} > 0$  and  $\vec{u}_{bq} = \vec{u}_b$  for  $\dot{\rho}_{bq} < 0$  (ANSYS Inc., ANSYS Fluent: User Guide, 2019).  $S_q$ , furthermore, includes the change in mass of phase  $q$  owing to heterogeneous reactions.

The phase interaction forces can be described as follows:

$$\vec{F}_{int,G} = -f_e \vec{F}_{GL} - (1 - f_e) \vec{F}_{GS} \quad (4)$$

$$\vec{F}_{int,L} = f_e (\vec{F}_{GL} - \vec{F}_{LS}) \quad (5)$$

where  $f_e = a_e/a_s$  marks the wetting efficiency. The wetting efficiency corresponds to the ratio of the particle surface covered with flowing liquid  $a_e$  to the entire specific particle surface area  $a_s$  (Colombo et al., 1976). It affects the impact of the interfacial interaction forces  $\vec{F}_{bq}$  on  $\vec{F}_{int,q}$ . The gas interaction with stagnant liquid is, hereby, treated as a direct interaction with the solid phase.  $\vec{F}_{bq}$  depends on the phase velocities with  $\vec{u}_s = \vec{0}\text{ m/s}$  and the interaction coefficients  $K_{bq}$ :

$$\vec{F}_{GS} = K_{GS} (\vec{u}_G - \vec{u}_s) \quad (6)$$

$$\vec{F}_{GL} = K_{GL} (\vec{u}_G - \vec{u}_L) \quad (7)$$

$$\vec{F}_{LS} = K_{LS} (\vec{u}_L - \vec{u}_s) \quad (8)$$

The expressions of  $K_{bq}$  consist of trickle bed properties, the modified gas velocity  $\vec{u}'_G = \vec{u}_G/\alpha$ , and the so-called Ergun parameters  $E_{\mu,q}$  and  $E_{\rho,q}$ :

$$K_{GS} = \frac{E_{\mu,G}(1 - \theta_G)^2 \mu_G}{\theta_G d_p^2} + \frac{E_{\rho,G}(1 - \theta_G) \rho_G |\vec{u}'_G|}{d_p} \quad (9)$$

$$K_{GL} = \frac{E_{\mu,G}(1 - \theta_G)^2 \mu_G}{\theta_G d_p^2} + \frac{E_{\rho,G}(1 - \theta_G) \rho_G |\vec{u}'_G - \vec{u}_L|}{d_p} \quad (10)$$

$$K_{LS} = \frac{E_{\mu,L}(1-\varepsilon)^2\mu_L}{\theta_L d_p^2} + \frac{E_{\rho,L}(1-\varepsilon)\rho_L}{d_p} \frac{|\vec{u}_L|}{d_p} \quad (11)$$

The bed structure is captured by the effective particle diameter  $d_p$  and the porosity  $\varepsilon$ . The modified gas velocity accounts for a higher pressure drop in regions with small gas saturation  $\alpha$ . In these regions, the gas phase needs to pass narrow liquid throats with increased flow resistance, cf. (Alopaeus et al., 2006).

Lappalainen et al. (2009; 2008; 2011) also originally incorporated  $\vec{u}'_G$  for the computation of  $\vec{F}_{GS} = K_{GS}(\vec{u}'_G - \vec{u}_s)$  and  $\vec{F}_{GL} = K_{GL}(\vec{u}'_G - \vec{u}_L)$ . Contrary to this, equation (6) and (7) use the common gas velocity  $\vec{u}_G$  by analogy with other multiphase models (Iliuta and Larachi, 2005; Kim et al., 2016; Janecki and Burghardt, 2014; Janecki et al., 2016; Fourati et al., 2013). Otherwise, we observed that the numerical computation of multiphase flow with species transport suffers from instability. For this reason, we propose  $\vec{u}'_G$  only in  $K_{GS} = f(\vec{u}'_G)$  and  $K_{GL} = f(\vec{u}'_G)$ , being aware that this might introduce slight changes in pressure drop.

The Ergun parameters are accessible by the phase specific tortuosity  $T_q$  of phase  $q$  and the friction factor  $f_\tau$  (Holub, 1990):

$$E_{\mu,q} = 72T_q^2 \quad (12)$$

$$E_{\rho,q} = 6f_\tau T_q^3 \quad (13)$$

The tortuosity addresses meanders of the fluid flow through the structure of the trickle bed (Zeiser, 2008). It augments with flow detour and deviation between inlet and outlet:

$$T_G = \frac{T_0 + 1}{2} + \alpha \left( \frac{T_0 + 1}{2} - 1 \right) \quad (14)$$

$$T_L = T_0 C_1^{(\alpha^2)} \quad (15)$$

The phase specific tortuosity can be estimated by means of gas saturation, the one-phase tortuosity  $T_0$ , and two constants  $C_1$  and  $C_2$ . Lappalainen et al. (2008) analyzed a comprehensive database and determined the values  $C_1 = 3.592$  and  $C_2 = 1.140$  for these constants. On the other hand, the one-phase tortuosity is valid for a one-phase fluid flow. Therefore,  $T_0$  and  $f_\tau$  can be expressed by equation (16) and (17):

$$T_0 = \sqrt{\frac{E_\mu}{72}} \quad (16)$$

$$f_\tau = \frac{E_\rho}{6T_0^3} \quad (17)$$

Originally defined universally (Ergun, 1952), the one-phase Ergun parameters  $E_\mu$  and  $E_\rho$  vary according to the bed particle properties. Macdonald et al. (1979) recommended  $E_\mu = 180$  and  $E_\rho = 4$  for rough particles, such as clay granulate. They moreover suggested a reduction of  $E_\mu$  and  $E_\rho$  by 15% if spherical particles are used. For this reason, the simulations herein encompass  $E_\mu = 153$  and  $E_\rho = 3.4$  for spherical clay granulate and the computation of phase interaction forces.

Wetting efficiency is, moreover, an important quantity for modeling interaction forces on multiphase flows in trickle bed reactors. Several correlations published in the literature have been developed either by semi-empirical analysis (Lappalainen et al., 2008; Ring and Missen, 1991; Al-Dahhan and Duduković, 1995; Burghardt et al., 1995) or neural networks (Larachi et al., 2001). Lappalainen et al. (2008) modeled  $f_e$  on the basis of experimental data which had been obtained predominantly for spherical bed particles:

$$f_e = 0,335 Re_L'^{0.185} Eö'^{-0.188} Ga_G'^{0.027} (1 + Fr_G)^{-0.014} \quad (18)$$

According to equation (18), the calculation of wetting efficiency requires the modified Reynolds number  $Re_L' = \rho_L d_p U_L / (\mu_L (1 - \varepsilon))$ , the modified Eötvös number  $Eö' = \rho_L g d_p^2 \varepsilon^2 / (\sigma (1 - \varepsilon)^2)$ , the modified Galileo number  $Ga_G' = \rho_G^2 g d_p^3 \varepsilon^3 / (\mu_G^2 (1 - \varepsilon)^3)$  and the Froude number  $Fr_G = U_G / \sqrt{g d_p}$ .

Analogous to the phase interaction forces, wetting efficiency also affects the aforementioned dispersion forces:

$$\vec{F}_{disp,G} = (1 - f_e) K_{GS} \vec{u}_{D,G} + f_e K_{GL} (\vec{u}_{D,G} - \vec{u}_{D,L}) \quad (19)$$

$$\vec{F}_{disp,L} = f_e K_{LS} \vec{u}_{D,L} - f_e K_{GL} (\vec{u}_{D,G} - \vec{u}_{D,L}) \quad (20)$$

Lappalainen et al. (2009) introduced  $\vec{F}_{disp,G}$  and  $\vec{F}_{disp,L}$  to cover dispersion effects pursuant to volume fraction gradients in 2D and 3D flow simulations. The drift velocity  $\vec{u}_{D,q}$  contains the local volume fraction gradients of phase  $q$ . If the fluid flow is two-dimensional and dominated by axial velocity  $u_{x,q}$ , the drift velocities can be described by the following expressions:

$$u_{Dy,G} = - \frac{S_m |\vec{u}_{x,G}|}{\theta_G} \frac{\partial \theta_G}{\partial y} \quad (21)$$

$$u_{Dy,L} = - \frac{S_m |\vec{u}_{x,L}|}{\theta_L} \frac{\partial \theta_L}{\partial y} \quad (22)$$

in which  $S_m$  refers to the spread factor of the CFD model. The spread factor characterizes the intensity of fluid dispersion in the trickle bed. Note that there is disparity between the model spread factor  $S_m$  and the experimental spread factor  $S$ . The experimental spread factor  $S$  is commonly measured by tracer experiments with a trickle bed completely wetted and flooded (Lappalainen et al., 2011). Due to the difference between these experiments and trickle bed applications which include only partially wetting of particles,  $S_m$  should be adjusted to  $S_m \approx 2S$  (Lappalainen et al., 2011). Equation (23) provides a semi-empirical correlation for  $S$  contingent on  $d_p$  and the particle shape factor  $\psi$ , developed by Baldi and Specchia (1976) in Lappalainen et al. (2011):

$$S = 0,015 \left( \frac{d_p}{m} \right)^{0.5} \psi^{-\frac{1}{3}} \quad (23)$$

In trickle bed reactors, the fluid flow is confined at reactor walls. The walls have considerable influence on local porosity if the tube-to-particle diameter  $D_R/d_p$  is in a range of 12 to 25 or smaller (Sarooha et al., 1998). The present simulation model comprehends a tube-to-particle diameter of  $D_R/d_p \approx 16$ . Therefore, a radial porosity profile was implemented to consider wall effects (Negri et al., 1999):

$$\varepsilon(\xi) = \bar{\varepsilon} + (1 - \bar{\varepsilon}) e^{-6\xi} \quad (24)$$

A simple exponential function approximates porosity in the vicinity of the wall, which tends towards  $\varepsilon \rightarrow 1$  for wall distance values of  $\xi = (R_R - r)/d_p \rightarrow 0$ .

### 1.3. Species transport

The species transport equations balance mass transfer and chemical conversion for every species involved, for both liquid and gas phases:

$$\begin{aligned} \frac{\partial}{\partial t} (\theta_q \rho_q \omega_q^I) + \nabla \cdot (\theta_q \rho_q \vec{u}_q \omega_q^I) \\ = -\nabla \cdot \theta_q \vec{J}_q^I + \dot{\rho}_{bq}^I + \theta_q \vec{R}_q^I + \vec{S}_q^I \end{aligned} \quad (25)$$



where  $\omega_q^l$  is the mass fraction of species  $l$  in phase  $q$ , which, furthermore, has to fulfill unity  $\sum_l \omega_q^l = 1$ . The first term on the right-hand side of equation (25) incorporates the diffusive flux due to mass fraction gradients and diffusivity  $D_q^l$  of component  $l$  in phase  $q$ :

$$\vec{J}_q^l = -\rho_q D_q^l \nabla \omega_q^l \quad (26)$$

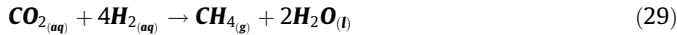
The second term denotes the species mass transfer per volume element  $\dot{\rho}_{bq}^l$  and, thus, absorption. Absorption can further be determined by Henry's law, which considers highly diluted solutes (Sattler and Feindt, 1995):

$$\dot{\rho}_{bq}^l = \frac{\dot{m}_{bq}^l}{V} = k_q a_l M^l \left( \frac{p_q^l}{K_H^{l,px}} - c_q^l \right) = -\dot{\rho}_{qb}^l \quad (27)$$

The calculation of  $\dot{\rho}_{bq}^l$  necessitates proper values of Henry's law constants  $K_H^{l,px}$ , the mass transfer coefficient  $k_q$ , and the interfacial area  $a_l$ . Algebraic correlations or neural networks enable the computation of the interfacial area (Iliuta et al., 1999). We implemented an algebraic, symmetric approach with the characteristic length of the gas phase  $x_G$  and the liquid phase  $x_L$  (ANSYS Inc., 2019):

$$a_l = \frac{6\theta_G \theta_L}{\theta_G x_L + \theta_L x_G} \quad (28)$$

The dissolution of  $H_2$  and  $CO_2$  enables the biochemical reaction in the liquid phase. For simplicity, the computational model assumes an irreversible and heterogeneous reaction into methane, in which the product arises only in the gas phase and  $H_2O$  is restricted to the liquid phase:



The homogeneous reaction rates  $R_L^l$  and the heterogeneous reaction rates  $S_q^l$  are simulated by simple second order kinetics including the stoichiometric factor  $\nu^l$  and the molecular weight  $M^l$  of species  $l$ . The reaction rate constant  $k_f$  is moreover calculated by the Arrhenius equation:

$$\frac{R_L^{CO_2}}{\nu^{CO_2} M^{CO_2}} = \frac{R_L^{H_2}}{\nu^{H_2} M^{H_2}} = \frac{S_G^{CH_4}}{\nu^{CH_4} M^{CH_4}} = \frac{R_L^{H_2O}}{\nu^{H_2O} M^{H_2O}} = k_f \cdot c_L^{CO_2} \cdot c_L^{H_2} \quad (30)$$

$$k_f = A_0 e^{-\frac{E_A}{RT}} \quad (31)$$

$A_0$  and  $E_A$  are the pre-exponential factor and the activation energy, respectively. Dependent on the flow case and pressure, an appropriate equation of state accomplishes closure of the equation system hereinabove.

#### 1.4. Domain extent and grid generation

The computational domain conforms to the experimental setup for validation. The trickle bed matches a cylinder with a top central liquid inlet. Fig. 2 delineates the domain extent and the structure of the applied computational grid. The liquid contact length  $L_L$  features a wall liquid volume fraction of  $\theta_L = 1\%$  and characterizes liquid dispersion in the trickle bed. Due to the central liquid inlet, the flow resembles an axisymmetric profile and can, thus, be reduced to 2D in present numerical calculations.

The 2D computational grid is implemented by an orthogonal lattice. The steep gradients in proximity of the wall and the liquid inlet are captured by higher grid resolution. In order to appraise the grid and its influence on liquid dispersion, a mesh independence study was performed taking  $L_L$  into account. The mesh inde-

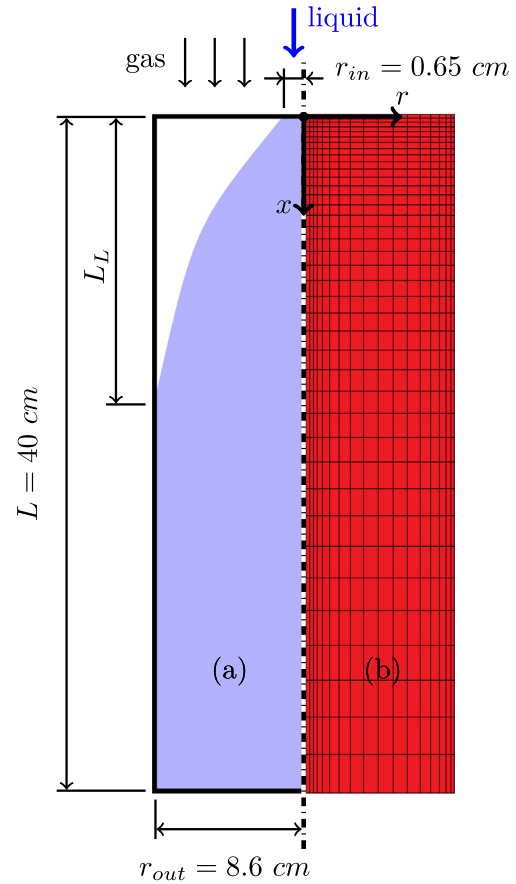


Fig. 2. Domain extent (a) and schematic image of the orthogonal structured grid (b) [ $L$ : reactor height;  $r_{out}$ : reactor radius;  $r_{in}$ : liquid inlet radius;  $L_L$ : liquid contact length]

pendence study was conducted with maximum liquid volume flow rates of  $\dot{V}_{L,in} = 10l/min$  which was anticipated to be the most stringent test. Three grids with  $N = 2280$ ,  $N = 6480$  and  $N = 11520$  cells and refinement factors of  $r_{12} = 1.5$  and  $r_{23} = 1.3$  were analyzed. The order of convergence  $p_{Grid}$  and the grid convergence index  $GCI$  were reckoned on the basis of Roache (1998) using generalized Richardson extrapolation:

$$p_{Grid}^{i+1} = \omega p_{Grid}^i + (1 - \omega) \frac{\ln \left( \frac{\left( \frac{p_{23}^i}{r_{23}^{Grid} - 1} \right) \cdot \frac{e_{12}}{e_{23}}}{\left( \frac{p_{12}^i}{r_{12}^{Grid} - 1} \right)} \right)}{\ln(r_{23})} \quad (32)$$

An iterative procedure examines the order of convergence for different grid refinement values including the relaxation factor  $\omega$  and the solution difference  $e_{j(j+1)} = L_{L,j} - L_{L,j+1}$ . The  $GCI$  represents the error band of the numerical solution in terms of grid refinement and, thus, accounts for grid uncertainty. It transfers the grid refinement results to grid doubling ( $r = 2$ ) and can be addressed to the coarse grid ( $GCI^{coarse}$ ) or the fine grid ( $GCI^{fine}$ ). Equation (33) and (34) estimate  $GCI$  with the relative error  $e = (L_{L,j} - L_{L,j+1})/L_{L,j+1}$  (Lotz et al., 1997):

$$GCI^{coarse} = F_s \cdot \frac{r^p |e|}{(r^p - 1)} \quad (33)$$

$$GCI^{fine} = F_s \cdot \frac{|e|}{(r^p - 1)} \quad (34)$$

$F_s$  is the safety factor. If the order of convergence is based on three or more grid solutions,  $F_s = 1.25$  is an appropriate value (Roache, 1998). Table 1 depicts the results of the systematic grid convergence test. The observed accuracy is of 2.26th-order. The grid with  $N = 6480$  exhibits a relative error smaller than 5% and a grid convergence index of  $GCI^{fine} \approx GCI^{coarse} \approx 11.1\%$ . This grid is assumed fine enough for the investigation of pseudo-continuous flow phenomena and, hence, it was chosen for the trickle bed simulations hereinafter.

### 1.5. Boundary conditions and model parameters

The present work comprises a hydrodynamic investigation with experimental validation on the one hand and the simulation of biological methanation in trickle bed reactors on the other hand.

The hydrodynamic investigation employs an incompressible water–air system. In this system, the liquid inlet is realized by a velocity inlet boundary condition. A pressure inlet condition at the remaining top surface area enables free entrance of the gas phase. The multiphase flow is, moreover, bordered by a no-slip wall and a symmetry boundary. The fluid departs from the pressure outlet at the bottom. The simulation of biological methanation involves species transport with a gas inlet molar composition of  $x_{H_2} = 0.8$  and  $x_{CO_2} = 0.2$ . Furthermore, a velocity inlet is implemented for both the gas and liquid inlet at the top in order to define a specific gas flow rate.

Table 2 contains the physical and chemical properties with respect to the different simulation scenarios. The physical properties of gas and liquid were determined by pure component and mixture analysis with the software ASPEN Plus® V8.8. In addition, extensive data by Sander (2015) and a mass transfer estimation by Burkhardt (2012) offer appropriate values for Henry and mass transfer coefficients, respectively.

The overall kinetics of biological methanation depend on several phenomena: convective and diffusive multiphase transport (hydrodynamics and gas–liquid mixing), species transport within each phase, interfacial species mass transfer (absorption), and the biologically induced methanation reaction. The major microkinetic limitation of biological methanation ensues from interfacial mass transfer, in particular hydrogen absorption (Jud et al., 1997). The implementation of detailed reaction mechanisms, therefore, plays a minor role in simulation of biological methanation as long as reaction rates exceed absorption rates. For this reason, the pre-exponential factor and activation energy were simply adjusted to very high reaction kinetics so that the overall process is limited by absorption.

## 2. Experimental setup

Thorough experimental analysis of liquid dispersion and holdup is pertinent to validation of the numerical model. Fig. 3 illustrates the experimental arrangement to measure these flow quantities. The pump conducts water from the storage to the top center of the trickle bed. The trickle bed itself is composed of spherical clay granulate which possesses an internal porous structure. The porous structure is beneficial for the settlement of microorganisms on the bed particle surface Burkhardt (2012). The particle diameter

**Table 2**  
Physical properties and simulation parameters.

trickle bed properties		
particle diameter and shape factor	$d_p = 1.07\text{cm}; \psi \approx 1$	measured
porosity	$\bar{\varepsilon} = 0.49$	measured
specific surface area	$a_s \geq 171\text{m}^2/\text{m}^3$	measured
Ergun coefficients	$E_\mu = 153; E_p = 3.4$	according to (Macdonald et al., 1979)
Empty bed tortuosity and friction factor	$T_0 = 1.4577; f_\tau = 0.1829$	according to eq. (16) and (17)
spread factor	$S_m = 2S = 0.31$	according to eq. (23)
<b>water–air system</b>		
liquid influx and velocity	$\dot{V}_L = 0.06 - 0.6\text{m}^3/\text{h}; u_{L,in} = 0.26 - 2.56\text{m/s}$	cocurrent flow
wetting efficiency	$f_e = 44.89 - 68.73\%$	according to eq. (18)
pressure	$p_{out} = p_{in} = 1.0135\text{bar}$	according to experiments
temperature	$T = 20^\circ\text{C} = 293.15\text{K}$	according to experiments
viscosity of gas and liquid phase	$\mu_G = 1.825 \cdot 10^{-5}\text{Pa} \cdot \text{s}; \mu_L = 1.002 \cdot 10^{-3}\text{Pa} \cdot \text{s}$	pure component analysis
density of gas and liquid phase	$\rho_G = 1.2\text{kg}/\text{m}^3; \rho_L = 998\text{kg}/\text{m}^3$	pure component analysis
surface tension	$\sigma = 0.073\text{kg}/\text{s}^2$	pure component analysis
<b>biological methanation</b>		
liquid influx and inlet velocities	$\dot{V}_L = 0.06\text{m}^3/\text{h}; u_{L,in} = u_{G,in} = 0.26\text{m/s}$	cocurrent flow
wetting efficiency	$f_e = 44.89\%$	according to eq. (18)
pressure	$p_{out} = 14\text{bar}$	–
temperature	$T = 65^\circ\text{C} = 338.15\text{K}$	–
viscosity of gas and liquid phase	$\mu_G = 1.49 \cdot 10^{-5}\text{Pa} \cdot \text{s}; \mu_L = 4.39 \cdot 10^{-4}\text{Pa} \cdot \text{s}$	mixture analysis
density of the liquid phase	$\rho_L = \rho_{H_2O} = 978\text{kg}/\text{m}^3$	pure component analysis
surface tension	$\sigma = 0.065\text{kg}/\text{s}^2$	mixture analysis
gas and liquid diffusivities	$D_G = 5.5 \cdot 10^{-6}\text{m}^2/\text{s}; D_L = 4.42 \cdot 10^{-9}\text{m}^2/\text{s}$	mixture analysis
Henry coefficients	$K_H^{H_2,px} = 8.487 \cdot 10^9\text{Pa}; K_H^{CO_2,px} = 4.263 \cdot 10^8\text{Pa}$	according to (Sander, 2015)
mass transfer coefficient	$k_q = 4 \cdot 10^{-6}\text{m/s}$	according to (Burkhardt, 2012)
phase-specific characteristic length	$x_G = x_L = d_p$	–
pre-exponential factor	$A_0 = 10^5\text{m}^3/(\text{mol} \cdot \text{s})$	adjusted
activation energy	$E_A = 10^3\text{J}/\text{mol}$	adjusted
equation of state	Redlich-Kwong	–

is  $d_p = 1.07\text{cm}$  and results in a tube-to-particle diameter ratio of  $D_R/d_p \approx 16$ . The specific area was estimated to be  $a_s = 171\text{m}^2/\text{m}^3$ , neglecting the particles inner porous structure. Hence, this value states a minimum and the actual specific surface area is considerably higher. At the bottom of the reactor, the water is separated into seven fractions. As a consequence, it is possible to quantify radial liquid flow profiles for a specific bed depth  $\Delta L$ .

The measurement of liquid holdup assimilates the method by Colombo et al. (1976), who measured the dynamic holdup  $\beta_{L,dyn}$  and the static holdup  $\beta_{L,stat}$  separately.  $\beta_{L,dyn}$  characterizes the flowing liquid which is constantly renewed by liquid influx. On

**Table 1**  
Liquid contact length  $L_L$  dependent on the cell number  $N$  [ $e$ : relative error;  $p_{Grid}$ : order of convergence;  $GCI$ : grid convergence index]

$j$	$N$	$L_{L,j}[\text{cm}]$	$ e $	$p_{Grid}$	$GCI$
1	2880	8.65	14.0%	2.26	29.1%
2	6480	10.05	4.2%		11.1%
3	11,520	10.50	–		5.8%

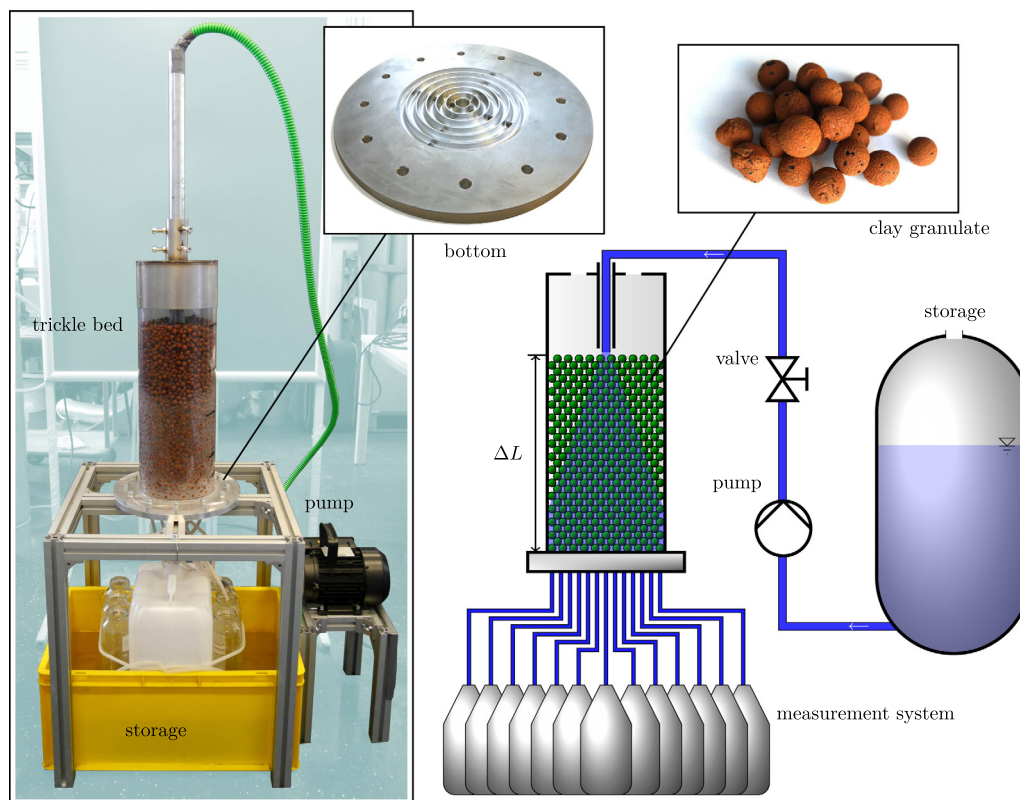


Fig. 3. Experimental setup to measure liquid dispersion for different bed depths  $\Delta L$  and liquid holdup.

the contrary,  $\beta_{L,stat}$  considers the stagnant liquid fraction in the trickle bed (Sattler and Feindt, 1995):

$$\beta_L = \frac{V_{L,total}}{V_R} = \frac{V_{L,stat} + V_{L,dyn}}{V_R} = \beta_{L,stat} + \beta_{L,dyn} \quad (35)$$

Dynamic holdup was measured by a sudden stop in water supply capturing the draining liquid in a measuring vessel for 20 min. On the other hand, static holdup was determined by the weight of the trickle bed after drainage.  $\beta_{L,stat}$  is inferred from the difference of the latter weight measurement and the weight of the dry trickle bed.

### 3. Results

The simulations were performed using the finite-volume commercial CFD code ANSYS® Fluent™ 18.0. This program provides the pressure-based solver PC-SIMPLE which represents a modification of the traditional SIMPLE algorithm for velocity–pressure coupling in terms of multiphase flows ANSYS Inc., (2019). PC-SIMPLE was applied in combination with an implicit second-order discretization scheme for time, a second-order upwind scheme for momentum, and a first-order upwind scheme for species and volume fraction. A least square cell based approach, moreover, approximated the gradients of the flow quantities.

The transient simulation was initialized with a pre-wetted bed ( $\alpha = 0.8$ ) and proceeded until steady state. We assumed steady state if the inlet and the outlet mass flow rate differed only by 0.1%, each with regard to consecutive time steps. The time step size varied from 0.0001 s to 0.4 s depending on the flow case and the solution state. If the residuals are less than  $10^{-3}$ , the calculation for a time step was deemed converging.

The under-relaxation factors were 0.1 for pressure, momentum, and volume fraction in the hydrodynamic investigation. Due to

smaller liquid influx, the simulation of biological methanation possesses smaller volume fraction gradients and, therefore, simulation stability allowed a pressure under-relaxation value of 1. However, stable computation of biological methanation required a step-by-step solution approach.

At first, only gaseous methane and pure water were conducted into the computational domain. As a result, the basic flow field evolved without absorption and reaction involved. Subsequently, the inlet molar fractions of hydrogen and carbon dioxide were slowly increased up to  $x_{H_2} = 0.8$  and  $x_{CO_2} = 0.2$ , still neglecting reaction into methane. The methanation reaction was activated only in the last step by an incremental augmentation in reaction rate. This bootstrap procedure allows the solution of the strongly coupled model equations. The phase interaction and dispersion forces in the phase-specific momentum equations were, furthermore, implemented by means of user-defined functions.

#### 3.1. Hydrodynamics

Phase distribution and interaction significantly affect mass transfer and reactor performance. For this reason, liquid dispersion and liquid holdup were placed under scrutiny in order to obtain the precision of the numerical computation with respect to experimental data. The experimental data comprise liquid volume flow rates of 0.12 m<sup>3</sup>/h, 0.3 m<sup>3</sup>/h, and 0.6 m<sup>3</sup>/h at trickle bed depths of 10 cm, 20 cm, 30 cm, and 40 cm. The radial local liquid mass flux  $\dot{m}_L/A$  was estimated in seven distinct chambers at the reactor bottom.

Fig. 4 portrays both experimental and simulation results of liquid dispersion. The experimental values were obtained by averaging several measurements with different random trickle bed particle arrangements. The error bars represent the affiliated standard deviations. As can be seen, the simulated mass flux coincides

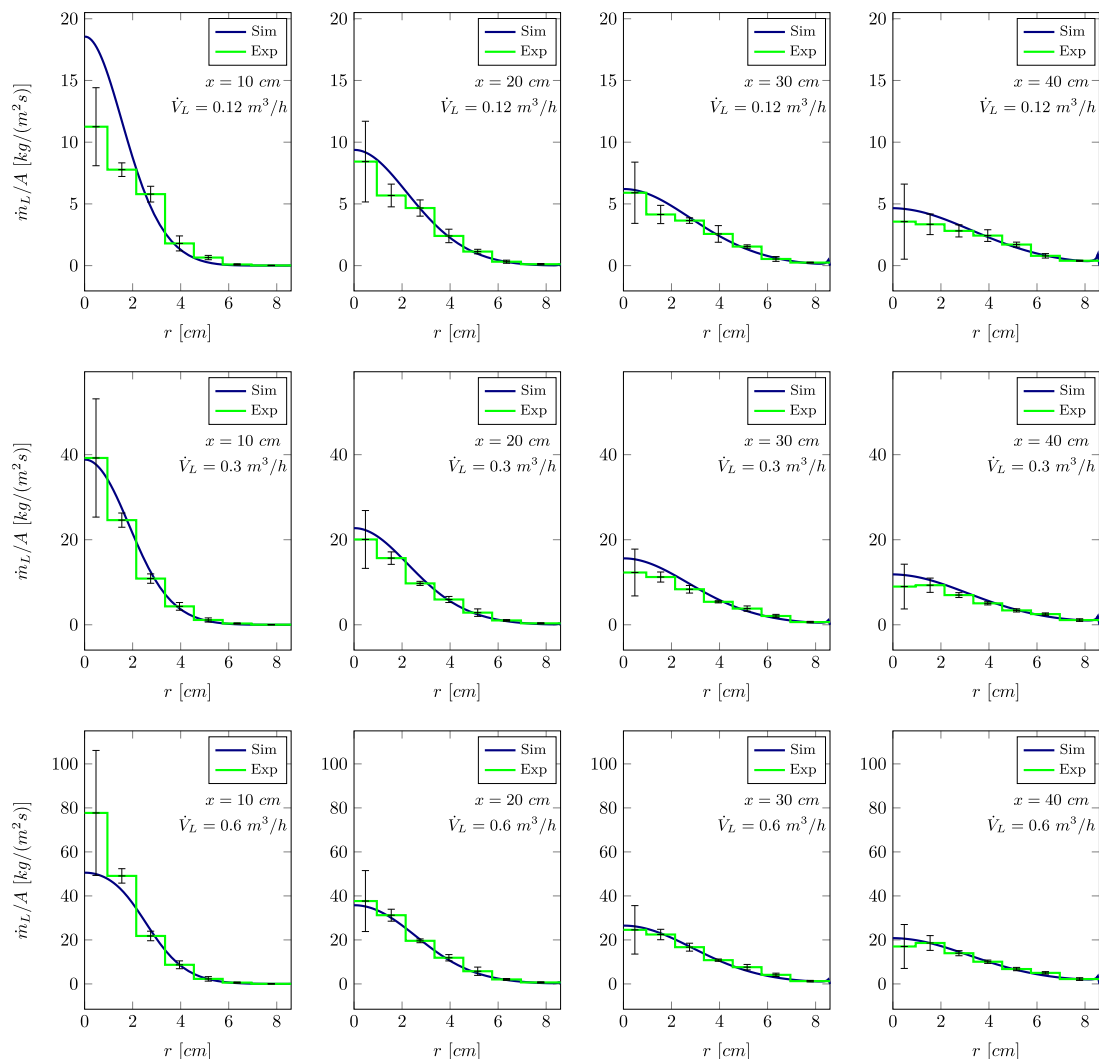


**Fig. 4.** Local liquid mass flux profiles  $\dot{m}_L/A$  dependent on the bed depth  $x$  and the overall liquid volume flow rate  $\dot{V}_L$  [Sim: Simulation; Exp: Mean value of several experimental measurements with error bars referring to standard deviation]

closely with experimental results except for the trickle bed depth of  $x = \Delta L = 10\text{ cm}$ . In the vicinity of the liquid inlet, the CFD model overestimates  $\dot{m}_L/A$  for the overall liquid flow rate of  $\dot{V}_L = 0.6\text{ m}^3/\text{h}$ . By contrast, an underestimation of  $\dot{m}_L/A$  is present for liquid flow rates of  $\dot{V}_L = 0.12\text{ m}^3/\text{h}$ . The differences may ensue from the strong gradients of flow quantities close to the liquid inlet. Hence, the numerical model is not able to capture these gradients and the respective flow profiles precisely over the entire operational range. Nevertheless, the over- and underestimation diminish within deeper depths.

In addition to these findings, the experiments display the dependence of local liquid flow on the bed particle arrangement. The standard deviation tends to increase in the center of the reactor. In particular in the first chamber with  $r \leq 1\text{ cm}$ , the standard deviation reaches values up to 80% of the mean value. These characteristics imply strong local differences in liquid distribution dependent on the trickle bed structure. They moreover indicate the corresponding scale of local maldistribution which seems to be on the same order of magnitude as the particle diameter ( $d_p = 1.07\text{ cm}$ ). This hypothesis was confirmed by additional experiments concerning the same particle arrangement. The results exhibit standard deviation values which are more than four times lower in comparison with experiments based on different bed par-

ticle arrangements (not shown). Consequently, the individual structure of the trickle bed has an appreciable influence on local liquid flow rates. This needs to be considered when applying the pseudo-continuous model to predict macroscopic flow phenomena and liquid dispersion in trickle bed reactors.

The uncertainty of the numerical prediction as well as any systematic errors can be visualized by a parity plot, which is delineated in Fig. 5. It compares the averaged mass flux  $(\dot{m}_L/A)_a$  for each chamber  $a$  with all measurements containing different bed particle arrangements, in total 672 data points. Approximately 90% of all data points are located within the  $\pm 50\%$  error band and 67% within the  $\pm 25\%$  error band. Only 36% of all data points remain within the  $\pm 10\%$  error band, which conforms to grid uncertainty. The data points with significant deviation can predominantly be attributed to the aforementioned over- and underestimation close to the liquid inlet. Furthermore, the prediction of low mass flux values suffers from appreciable scattering. This might originate from experimental measuring uncertainty.

In addition to liquid dispersion, liquid holdup was analyzed and validated. Fig. 6 portrays liquid holdup for overall liquid volume flow rates in between  $\dot{V}_L = 0.06\text{ m}^3/\text{h}$  and  $\dot{V}_L = 0.6\text{ m}^3/\text{h}$ . The error bars display the standard deviation and signify measurement uncertainty (up to 6%). The simulation and experimental results



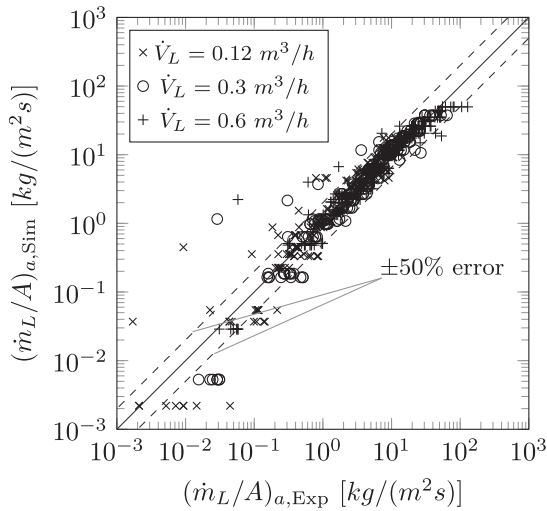


**Fig. 5.** Parity plot of simulated (Sim) and measured (Exp) mass flux values  $(\dot{m}_L/A)_a$  for each chamber **a**.

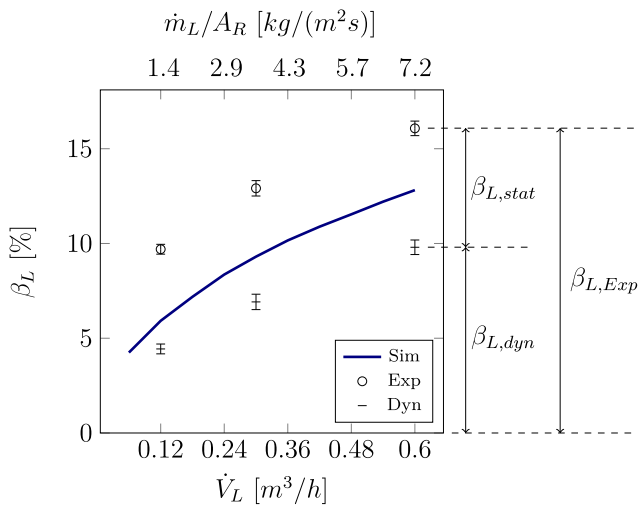


**Fig. 6.** Liquid holdup  $\beta_L$  dependent on overall liquid volume flow rate  $\dot{V}_L$  and overall mass flux  $\dot{m}_L/A_R$  [ $\beta_{L,stat}$ : static liquid holdup;  $\beta_{L,dyn}$ : dynamic liquid holdup;  $\beta_{L,Exp}$ : total measured liquid holdup; Sim: Simulation]

possess similar augmentation in total liquid holdup with increasing  $\dot{V}_L$ . This augmentation is mainly induced by the dynamic constituent  $\beta_{L,dyn}$ . However, for clay granulate, the absolute value of  $\beta_{L,Exp}$  differs considerably from simulation results.  $\beta_{L,Exp}$  is much higher than simulated  $\beta_L$ . Hence, the trickle bed contains much more liquid. In all probability, the discrepancy refers to the internal porosity of clay granulate which facilitates water deposition within bed particles. Water seeps into the porous structure of clay granulate and is trapped within inner pores due to capillary forces. This effect contributes appreciably to  $\beta_{L,stat}$ . The presented numerical model considers the total averaged porosity  $\bar{\varepsilon}$  containing both external and internal porosity but neglects the capillary forces inside the pores of clay granulate. As a consequence, the model is not able to capture water deposits within the pores and static liquid holdup is underestimated in the simulation. Modelling of such capillary forces would require intimate knowledge of the porous structure and should include essential pore characteristics, such as pore diameter and shape.

In summary, in spite of the holdup underestimation of clay granulate and the uncertainty regarding local inhomogeneity, the

Eulerian-Eulerian multiphase model provides a reasonable approximation of macroscopic multiphase flows in trickle bed reactors.

### 3.2. Biological methanation

On the basis of the hydrodynamic investigation, the simulation of biological methanation with species transport was performed. Herein, a velocity inlet boundary condition realized the gas influx explicitly. Using uniform profiles of the gas inlet velocity  $u_{G,in}$ , the simulation enables cocurrent ( $u_{G,in} > 0$ ) or countercurrent flow ( $u_{G,in} < 0$ ). Preliminary studies provide the corresponding gas stream lines dependent on  $u_{G,in}$  (Fig. 7). If the gas inlet velocity exceeds a certain threshold level ( $|u_{G,in}| \geq u_{G,in}^{crit}$ ), the gas perfuses the trickle bed without appreciable detour. However, if the gas inlet velocity remains below the critical gas inlet velocity  $u_{G,in}^{crit}$ , the interaction with the liquid phase dominates overall gas flow.  $u_{G,in}^{crit}$  depends on the physical and chemical properties of the system, such as domain geometry, fluid properties, porosity, bed particle diameter, and the liquid influx. For  $|u_{G,in}| < u_{G,in}^{crit}$ , the liquid entrains the bulk gas phase close to the middle axis and ‘pulls’ it out of the domain. As a result, backflow of gas arises at the pressure outlet and in proximity of the wall in order to balance gas mass

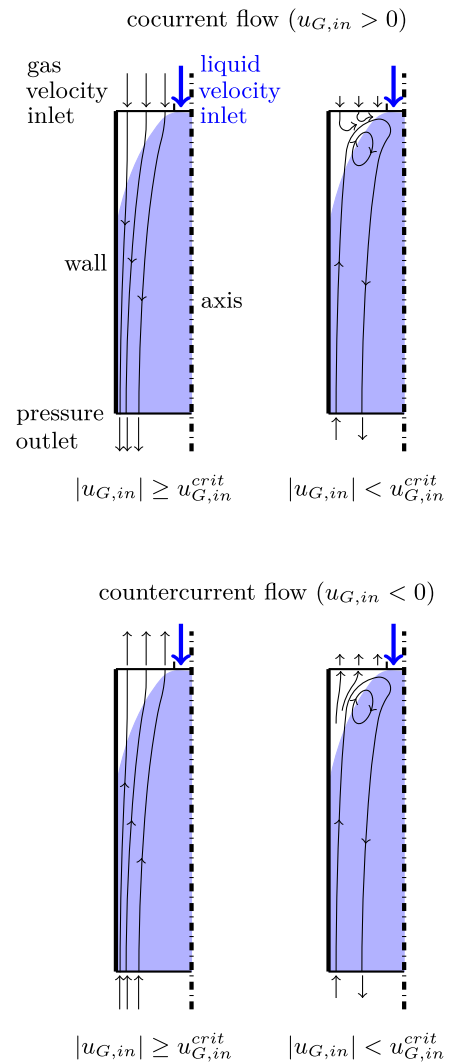


**Fig. 7.** Schematic flow profiles with the boundary conditions used and the gas stream lines of co- and countercurrent flow [ $u_{G,in}$ : gas inlet velocity;  $u_{G,in}^{crit}$ : critical gas inlet velocity]

transfer. This backflow prevents the development of well-defined co- or countercurrent flow and, therefore, should be avoided. For this reason, biological methanation was simulated applying  $u_{G,in} = 0.26 \text{ m/s} \geq u_{G,in}^{crit}$  in cocurrent flow.

As can be seen, the gas inlet boundary condition affects the gas flow profile materially. Owing to the coupling of gas flow with gas species transport and distribution, it also affects absorption and biochemical conversion into methane. For this reason, proper implementation of the gas inlet is of utmost importance in order to predict biological methanation accurately.

The critical gas inlet velocity characterizes the lower limit on gas flow rates in the present computational setup. In terms of the liquid phase, the model does not possess a lower limit. The upper limit on gas and liquid inlet flow rates may be imposed by computational instability since strong velocity gradients appear in the vicinity of the liquid inlet and impede the computational procedure. For this reason, an augmentation in gas and liquid inlet velocities – beyond  $u_{L,in} = u_{G,in} = 2.56 \text{ m/s}$  – should follow an increase in grid resolution to resolve these gradients adequately. Additionally, we recommend lower underrelaxation parameters to facilitate convergence.

Fig. 8 depicts contour plots of the liquid volume fraction and species molar fractions in the computational domain. The incoming liquid disseminates radially in the trickle bed. As a consequence, the liquid volume fraction exhibits high values and steep gradients close to the inlet, whereas it features smoother graduation in the vicinity of the outlet. This flow profile affects mass transfer and biochemical conversion appreciably.

Due to enhanced gas–liquid mixing in the lower part of the trickle bed, mass transfer is facilitated. The decrease in the gaseous  $\text{CO}_2$  molar fraction, thus, correlates with gas–liquid mixing. In the liquid phase, the  $\text{CO}_2$  molar fraction possesses slightly higher values far from liquid inlet. In these outer regions, the small portion of liquid remains almost stagnant which enables an accumulation of  $\text{CO}_2$ . On the contrary, the liquid flow in the inner region entrains  $\text{CO}_2$  out of the domain and leads to a vanishing liquid  $\text{CO}_2$  molar fraction in the center. In comparison with carbon dioxide, hydrogen absorption is much slower inducing an augmentation in the  $\text{H}_2$  molar fraction in the gas phase. By contrast, the liquid  $\text{H}_2$  molar fraction tends towards zero within the entire domain (not shown). Owing to fast reaction kinetics, liquid hydrogen reacts instantaneously.

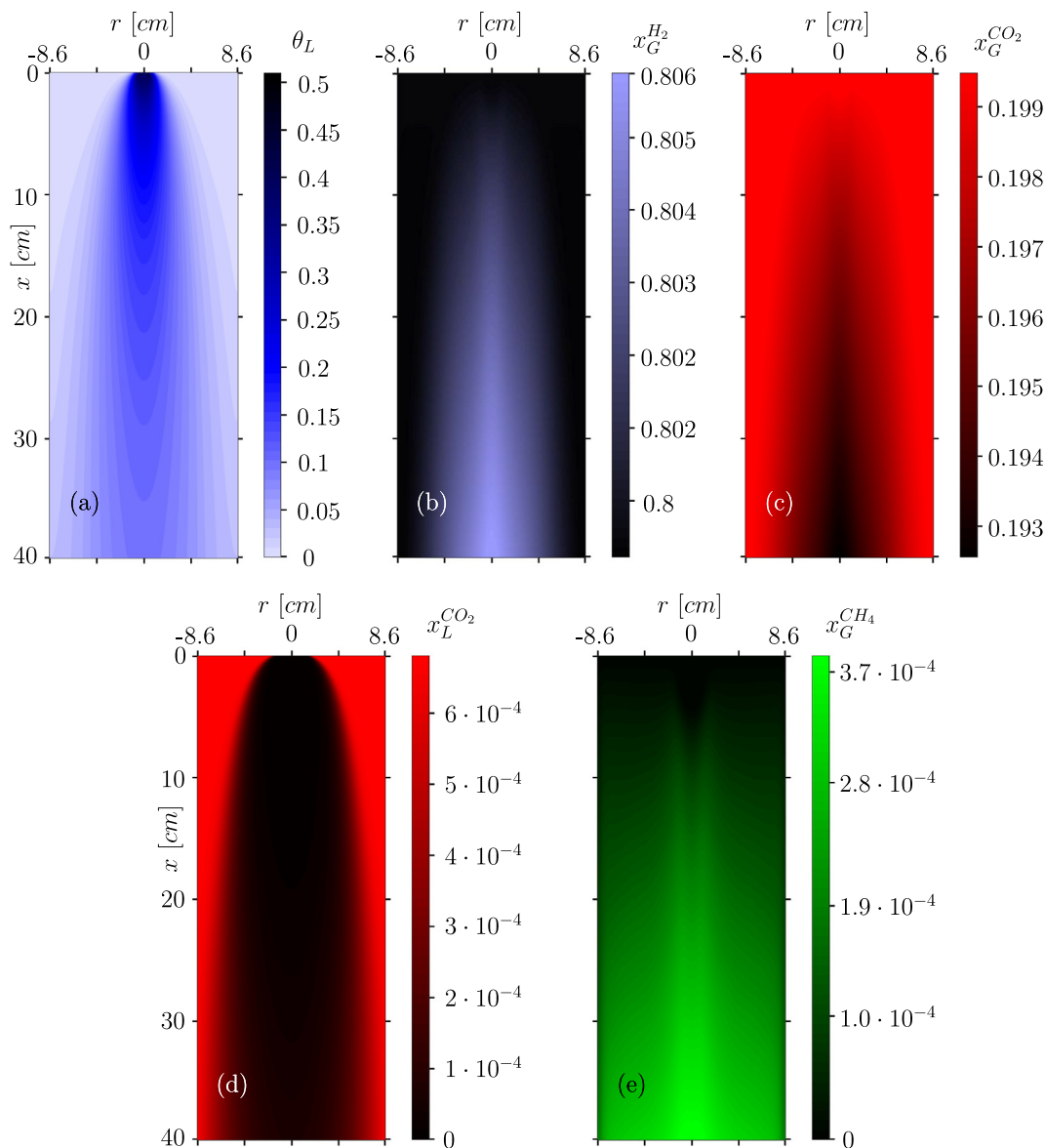


**Fig. 8.** Liquid volume fraction (a), gaseous hydrogen molar fraction (b), gaseous carbon dioxide molar fraction (c), liquid carbon dioxide molar fraction (d), and gaseous methane molar fraction (e).

**Table 3**Specific surface area  $a_s$ , methane production rate  $MPR$ , gas hourly space velocity  $GHSV$ , retention time  $\tau$ , and methane concentration  $y^{CH_4}$  from simulation and literature data.

	Gas feed composition	operation	$a_s$	$MPR$	$GHSV$	$\tau$	$y^{CH_4}$
			$\left[\frac{m^2}{m^3}\right]$	$\left[\frac{m^3_{CH_4}}{m^3d}\right]$	$\left[\frac{m^3}{m^3h}\right]$	$[h]$	$[vol. - \%]$
Simulation	80% H <sub>2</sub> ; 20% CO <sub>2</sub>	–	171	6.6	2327	$4.3 \cdot 10^{-3}$	0.03
Burkhardt and Busch (2013)	80% H <sub>2</sub> ; 20% CO <sub>2</sub>	product gas recycle	305	1.2	0.3	2.3	94
Rachbauer et al. (2016)	Biogas (36–42% CO <sub>2</sub> ; 58–64% CH <sub>4</sub> ); H <sub>2</sub> /CO <sub>2</sub> = 4/1	biogas upgrading	313	2.5	0.7	1.4	84
Burkhardt et al. (2015)	80% H <sub>2</sub> ; 20% CO <sub>2</sub>	product gas recycle	305	1.2	0.3	4	98
Strübing et al. (2017)	H <sub>2</sub> /CO <sub>2</sub> = 3.75 – 4.00	–	313–859	15.4	3.2	0.3	98
Dupnock and Deshusses (2017)	67% H <sub>2</sub> ; 16% CO <sub>2</sub> ; 17% N <sub>2</sub>	–	600	38	0.05	0.2	44

neously with excess liquid carbon dioxide. The heterogeneous reaction into methane moreover results in increasing gaseous CH<sub>4</sub> molar fractions along the trickle bed depth. In Fig. 8e, the highest CH<sub>4</sub> molar fractions arise close to the center of the domain. As mentioned before, this may occur from intense gas–liquid mixing and slow methane accumulation in the gas phase. In addition, higher gaseous H<sub>2</sub> molar fraction values improve hydrogen absorption and, therefore, methanation.

The contour plots provide detailed insight into biological methanation in the trickle bed under present assumptions. The deductions from simulation data are fair but are hard to show experimentally. For this reason, validation of biological methanation was performed based on literature values with respect to overall balances. Table 3 itemizes the specific surface area  $a_s$ , the methane production rate  $MPR$ , the gas hourly space velocity  $GHSV$ , the retention time  $\tau$ , and the product gas concentration of methane  $y^{CH_4}$  from the simulation and the literature. The  $MPR$  relates the methane production to the global reactor volume  $V_R$  whereas the  $GHSV$  includes the total gas influx  $\dot{V}_{G,in}$  (Thema et al., 2019).

$$MPR = \frac{\dot{V}_{CH_4,out} - \dot{V}_{CH_4,in}}{V_R} \quad (36)$$

$$GHSV = \frac{\dot{V}_{G,in}}{V_R} \quad (37)$$

As can be seen, the predicted methane production rate is of the same order of magnitude as experimental values. It slightly exceeds the experimental data of Burkhardt and Busch (2013), Rachbauer et al. (2016), and Burkhardt et al. (2015). Owing to very high  $GHSV$  for the applied gas inlet velocity of  $u_{G,in} = 0.26 \text{ m/s} \geq u_{G,in}^{crit}$  and no product gas recycle, the simulation features only a low retention time. As a result, only a small portion of hydrogen and carbon dioxide reacts into methane ( $y^{CH_4} \approx 3 \cdot 10^{-4} \text{ vol.} - \%$ ). On the other hand, this conduces to high hydrogen partial pressure throughout the entire trickle bed which enhances hydrogen absorption and may explain the remarkable methane production rate of  $MPR = 6.6 \text{ m}^3_{N,CH_4}/(\text{m}^3\text{d})$ . Strübing et al. (2017) and Dupnock and Deshusses (2017) published even higher productivity with  $MPR = 15.4 \text{ m}^3_{N,CH_4}/(\text{m}^3\text{d})$  and  $MPR = 38 \text{ m}^3_{N,CH_4}/(\text{m}^3\text{d})$ , respectively. Strübing et al. (2017) analyzed a trickle bed with two types of particles and Dupnock and Deshusses (2017) applied an open pore polyurethane foam trickling filter. In comparison with the simulation and the other publications, the specific surface area of the packing was much higher, which seems to enhance the methanation process.

#### 4. Conclusion

The present work promotes a comprehensive CFD model, which includes cocurrent multiphase flow, absorption, and reaction mechanisms in trickle bed reactors dedicated to biological metha-

nation. Based on the results obtained, the following conclusions can be drawn:

- Although the pseudo-continuous model neglects local inhomogeneity, the simulation of liquid dispersion is in satisfactory agreement with averaged macroscopic flow profiles from experimental data. The main deviation is located close to the liquid inlet. The proximate liquid influx induces strong gradients of flow quantities which results in an overestimation of mass flux for high volume flow rates and an underestimation for low volume flow rates.
- The computation of liquid holdup resembles the experimental augmentation with increasing liquid influx. However, the internal porosity of clay granulate is not considered by the mathematical approach and, therefore, static liquid holdup is underrated considerably.
- The simulation of gaseous species absorption and subsequent biological methanation demonstrates the dependence of biochemical conversion on gas and liquid flow conditions. The strong fluid mixing in the vicinity of the outlet enhances hydrogen absorption and its reaction into methane. However, methane concentration is limited to diminutive values because of low retention time. Nevertheless, a methane production rate of  $MPR = 6.6 \text{ m}^3_{N,CH_4}/(\text{m}^3\text{d})$  is on the same order of magnitude as literature data.

In order to increase the accuracy of the simulation results, our future work will focus on the implementation of more precise reaction kinetics (enzyme kinetics) and the incorporation of pore capillary forces into the computational model. Additionally, further validation of biological methanation and pressure drop, as well as the model adjustment to countercurrent operation with low gas retention time, will be addressed. The latter will include modelling of the head space above the trickle bed and the bottom portion with gas–liquid separation.

In conclusion, the numerical multiphase model provides a fair approximation of hydrodynamics and mass transfer for biological methanation and allows for fast parameter variations. This may reduce the expensive and long-lasting experimental procedures of biological methanation and accelerate its optimization.

#### Acknowledgments

The authors would like to thank the German Federal Ministry for Economic Affairs and Energy for financial support (Project: ORBIT; Grant-ID: 03ET6125B). Moreover, special thanks go to Victoria Jackiw for proofreading.

#### Appendix A. Supplementary data

Supplementary data to this article can be found online at <https://doi.org/10.1016/j.ces.2020.115847>.

## References

- Thema, M., Sterner, M., Lenck, T., Götz, P., 2016. Necessity and Impact of Power-to-gas on Energy Transition in Germany. *Energy Procedia*, 392–400. <https://doi.org/10.1016/j.egypro.2016.10.129>.
- Götz, M., Lefebvre, J., Friedemann, M., Manuel, G., Graf, F., Bajohr, S., Reimert, R., Kolb, T., 2016. Renewable Power-to-Gas : A technological and economic review. *Renew. Energy*, 85, 1371–1390. <https://doi.org/10.1016/j.renene.2015.07.066>.
- Colombo, J., Baldi, G., Sicardi, S., 1976. Solid-liquid contacting effectiveness in trickle bed reactors. *Chem. Eng. Sci.* 31, 1101–1108.
- Coutanceau, C., Baranton, S., Audichon, T., 2017. *Hydrogen Electrochemical Production*. Academic Press.
- Sterner, M., Stadler, I., 2014. *Energiespeicher - Bedarf. Integration*, Springer-Verlag, Berlin Heidelberg, Technologien.
- Thema, M., Weidlich, T., Hörl, M., Bellack, A., Mörs, F., Hackl, F., Kohlmayer, M., Gleich, J., Stabenau, C., Trabold, T., Neubert, M., Ortlo, F., Brotsack, R., Schmack, D., Huber, H., Hafenbradl, D., Karl, J., Sterner, M., 2019. Biological CO<sub>2</sub>-Methanation: An Approach to Standardization. *Energies*, 12, 1–32. <https://doi.org/10.3390/en12091670>.
- Ranade, V.V., Chaudhari, R.V., Gunjal, P.R., 2011. *Trickle Bed Reactors: Reactor Engineering & Applications*. Elsevier.
- M. Burkhart, Die Leistungsfähigkeit anaerober Rieselbettreaktoren zur Methanisierung flüssiger und gasförmiger organischer Verbindungen durch biofilmgebundene methanogene Archaeen, Brandenburgischen Technischen Universität Cottbus, 2012.
- Rachbauer, L., Voitl, G., Bochmann, G., Fuchs, W., 2016. Biological biogas upgrading capacity of a hydrogenotrophic community in a trickle-bed reactor. *Appl. Energy*, 180, 483–490. <https://doi.org/10.1016/j.apenergy.2016.07.109>.
- Burkhart, M., Busch, G., 2013. Methanation of hydrogen and carbon dioxide. *Appl. Energy*, 111, 74–79. <https://doi.org/10.1016/j.apenergy.2013.04.080>.
- Burkhart, M., Koschack, T., Busch, G., 2015. Biocatalytic methanation of hydrogen and carbon dioxide in an anaerobic three-phase system. *Bioresour. Technol.* 178, 330–333.
- Strübing, D., Huber, B., Leubhn, M., Drewes, J.E., Koch, K., 2017. High performance biological methanation in a thermophilic anaerobic trickle bed reactor. *Bioresour. Technol.* 245, 1176–1183.
- Dupnock, T.L., Deshusses, M.A., 2017. High-Performance Biogas Upgrading Using a Biotrickling Filter and Hydrogenotrophic Methanogens. *Appl. Biochem. Biotechnol.* 183, 488–502. <https://doi.org/10.1007/s12010-017-2569-2>.
- Weidlich, T., Neubert, M., Dillig, M., Karl, J., 2018. Biological methanation in a trickle-bed reactor. *Eur. Biomass Conf. Exhib. Proc. 26thEUBCE*, 596–598.
- Bär, K., Mörs, F., Götz, M., Graf, F., 2015. Vergleich der biologischen und katalytischen Methanisierung für den Einsatz bei PtG-Konzepten. *Gwf-Gas*, 156, 466–473.
- Ergun, S., 1952. Fluid flow through packed columns. *Chem. Eng. Prog.* 48, 89–94.
- Attou, A., Boyer, C., Ferschneider, G., 1999. Modelling of the hydrodynamics of the cocurrent gas – liquid trickle flow through a trickle-bed reactor. *Chem. Eng. Sci.* 54, 785–802.
- Iliuta, I., Larachi, F., 2005. Modelling the Hydrodynamics of Gas-Liquid Packed Beds via Slit Models: A Review. *Int. J. Chem. React. Eng.* 3.
- Alopaeus, V., Hyninen, K., Aittamaa, J., Manninen, M., 2006. Modeling of Gas-Liquid Packed-Bed Reactors with Momentum Equations and Local Interaction Closures. *Ind. Eng. Chem. Res.* 45, 8189–8198. <https://doi.org/10.1021/ie0606338>.
- Lappalainen, K., Manninen, M., Alopaeus, V., 2009. CFD modeling of radial spreading of flow in trickle-bed reactors due to mechanical and capillary dispersion. *Chem. Eng. Sci.* 64, 207–218. <https://doi.org/10.1016/j.ces.2008.10.009>.
- Kim, J., Pham, D.A., Lim, Y.-I., 2016. Gas–liquid multiphase computational fluid dynamics (CFD) of amineabsorption column with structured-packing for CO<sub>2</sub> capture. *Comput. Chem. Eng.* 88, 39–49. <https://doi.org/10.1016/j.compchemeng.2016.02.006>.
- Janecki, D., Szczotka, A., Burghardt, A., Bartelmus, G., 2016. Modelling wet-air oxidation of phenol in a trickle-bed reactor using active carbon as a catalyst. *J. Chem. Technol. Biotechnol.* 91 (3), 596–607. <https://doi.org/10.1002/jctb.4610>.
- ANSYS Inc., ANSYS Fluent: User Guide, (2019).
- Lappalainen, K., Alopaeus, V., Manninen, M., Aittamaa, J., 2008. Improved Hydrodynamic Model for Wetting Efficiency, Pressure Drop, and Liquid Holdup in Trickle-Bed Reactors. *Ind. Eng. Chem. Res.* 47, 8436–8444. <https://doi.org/10.1021/ie8003754>.
- Lappalainen, K., Gorshkova, E., Manninen, M., Alopaeus, V., 2011. Characteristics of liquid and tracer dispersion in trickle-bed reactors : Effect on CFD modeling and experimental analyses. *Comput. Chem. Eng.* 35, 41–49. <https://doi.org/10.1016/j.compchemeng.2010.06.006>.
- Janecki, D., Burghardt, A., 2014. Influence of the porosity profile and sets of Ergun constants on the main hydrodynamic parameters in the trickle-bed reactors. *Chem. Eng. J.* 237, 176–188. <https://doi.org/10.1016/j.ces.2013.09.102>.
- Janecki, D., Burghardt, A., Bartelmus, G., 2016. Parametric sensitivity of a CFD model concerning the hydrodynamics of trickle-bed reactor (TBR). *Chem. Process Eng.* 37, 97–107. <https://doi.org/10.1515/cpe-2016-0010>.
- Fourati, M., Roig, V., Raynal, L., 2013. Liquid dispersion in packed columns : Experiments and numerical modeling. *Chem. Eng. Sci.* 100, 266–278. <https://doi.org/10.1016/j.ces.2013.02.041>.
- Holub, R.A., 1990. Hydrodynamics of trickle bed reactors. Washington University.
- Zeiser, T., 2008. Simulation und Analyse von durchströmten Kugelschüttungen in engen Rohren unter Verwendung von Hochleistungsrechnern. Friedrich-Alexander-Universität Erlangen-Nürnberg.
- Macdonald, I.F., Mow, K., Dullien, F.A.L., 1979. Flow through Porous Media—the Ergun Equation Revisited. *Ind. Eng. Chem. Fundam.* 18, 199–208.
- Ring, Z.E., Missen, R.W., 1991. Trickle-Bed Reactors : Tracer Study of Liquid Holdup and Wetting Efficiency at High Temperature and Pressure. *Can. J. Chem. Eng.* 69, 1016–1020.
- Al-Dahhan, M.H., Duduković, M.P., 1995. Catalyst wetting efficiency in trickle-bed reactors at high pressure. *Chem. Eng. Sci.* 50, 2377–2389.
- Burghardt, A., Bartelmus, G., Jaroszyński, M., Kołodziej, A., 1995. Hydrodynamics and mass transfer in a three-phase fixed-bed reactor with cocurrent gas–liquid downflow. *Chem. Eng. J. Biochem. Eng. J.* 58, 83–99.
- Larachi, F., Belfares, L., Grandjean, B.P.A., 2001. Prediction of liquid-solid wetting efficiency in trickle flow reactors. *Int. Commun. Heat Mass Transf.* 28, 595–603.
- Baldi, G., Specchia, V., 1976. Distribution and Radial Spread of Liquid in Packed Towers with Two-Phase Concurrent Flow: Effect of Packing Shape and Size. *Quad. Dell'ingegnere Chim. Ital.* 12, 107–112.
- Saroha, A.K., Nigam, K.D.P., Saxena, A.K., Kapoor, V.K., 1998. Liquid Distribution in Trickle-Bed Reactors. *AIChE J.* 44, 2044–2052.
- Negrini, A.L., Fuelber, A., Freire, J.T., Thomeo, J.C., 1999. Fluid dynamics of air in a packed bed: velocity profiles and the continuum model assumption. *Brazilian J. Chem. Eng.* 16, 421–432. <https://doi.org/10.1590/S0104-66321999000400010>.
- Sattler, K., Feindt, H.J., 1995. *Thermal Separation Processes*. VCH Verlagsgesellschaft mbH, Weinheim.
- Iliuta, I., Larachi, F., Grandjean, B.P.A., Wild, G., 1999. Gas-liquid interfacial mass transfer in trickle-bed reactors : state-of-the-art correlations. *Chem. Eng. Sci.* 54, 5633–5645.
- Roache, P.J., 1998. Verification of Codes and Calculations. *AIAA J.* 36, 696–702.
- Lotz, R.D., Thompson, B.E., Konings, C.A., 1997. Numerical uncertainties in transonic flow calculations for aerofoils with blunt trailing edges. *Int. J. Numer. Methods Fluids*, 24, 355–373.
- Sander, R., 2015. Compilation of Henry ' s law constants (version 4.0) for water as solvent. *Atmos. Chem. Phys.* 15, 4399–4981. <https://doi.org/10.5194/acp-15-4399-2015>.
- Jud, G., Schneider, K., Bachofen, R., 1997. The role of hydrogen mass transfer for the growth kinetics of *Methanobacterium thermoautotrophicum* in batch and chemostat cultures. *J. Ind. Microbiol. Biotechnol.* 19, 246–251.